Journal of Applied Mechanics Vol.8, pp.267-276 (August 2005) JSCE

High-Speed Contact-Impact Simulations with Lagrangian and Eulerian Hydrocode

Rafael Doig*, Shigenobu Okazawa** and Masahiko Fujikubo***

*Doctorate Student, Hiroshima University (1-4-1, Kagamiyama, Higashi-Hiroshima 739-8527)
**Associate Professor, Hiroshima University (1-4-1, Kagamiyama, Higashi-Hiroshima 739-8527)
***Professor, Hiroshima University (1-4-1, Kagamiyama, Higashi-Hiroshima 739-8527)

In a high-speed impact, both projectile and target experience an extreme distortion. A simulation in Eulerian formulation is therefore favorized. Contact-impact with Lagragian meshes are also presented. Focused topics here are Lagrangian and Eulerian formulation of a continuum media, plasticity flow, material separation due to failure or penetration, contact algorithm, 1-point integrated elements for computational time performance.

Key Words : *Lagrangian and Eulerian hydrocode, high-speed impact, contact, penetration, elastoplasticity, 1-point element integration*

1. Introduction

High-speed impact analyses are being widely researched. Research on numerical methods like, smooth particle hydrodynamics, Lagrangian finite element method with element erosion, discrete elements and split-element method has been carried out by many other authors. However, there are less references by using Eulerian hydrocodes. Problems like large deformation with mesh distortion, contact, penetration and 1-point integrated elements have been treated here. The former pointed problem is easiest overcame by using a fixed mesh. Additionally to the Lagrangian formulation used by conventional hydrocodes, an Eulerian or second order advective step has been programmed. Later step transports the material through the re-meshed mesh.

An Eulerian hydrocode allows material separation caused during penetration. Programming procedures have been implemented for fracture models like plastic strain condition model and Johnson-Cook fracture model. Different from contact problems in Lagrangian Hydrocodes, where the penalty method is most popular, in an Eulerian Hydrocode mixture theories have been studied. The mixture theory bases on multi-material elements in which materials are mixed.

The J_2 plasticity theory, implemented in this Hydrocode, confirms its suitability for metal plasticity. Further, for a computational time improvement 1-point integrated elements with hourglass control method have been implemented. The selected hourglass control procedure shows a remarkable time performance keeping good accuracy and avoiding hourglassing.

2. Eulerian Formulation

During the material time derivative is used in the standard Lagrangian formulation, the spatial time derivative is applied in the Eulerian formulation. In other words, a Lagrange mesh moves with the material as an Eulerian mesh keeps fixed in the space letting pass the material through its cells. Here a compact review of that part of continuum mechanics is presented. If interested, a broad variety of good resources is available, i.e. [1) 2) 3)] and others.

For an arbitrary solution variable ϕ, the relation between the material and the spatial time derivatives is

$$\frac{D\phi}{Dt} = \frac{\partial \phi}{\partial t} + \boldsymbol{v} \cdot (\nabla \phi) \tag{1}$$

where $D\phi/Dt$ is the material time derivative and $\partial\phi/\partial t$ the spatial time derivative of the solution variable ϕ. The difference makes the convective term $\boldsymbol{v} \cdot (\nabla \phi)$.

It can be shown that the Eulerian governing equations, namely the mass, momentum and energy conservation equations follow the general conservative form

$$\frac{\partial \phi}{\partial t} + \nabla \cdot \boldsymbol{\Phi} = \boldsymbol{S} \tag{2}$$

where $\boldsymbol{\Phi}$ is a flux function and $\boldsymbol{S}$ is a source.

The operator split method splits eq. (2) into two equations, namely

$$\frac{\partial \phi}{\partial t} = \boldsymbol{S} \tag{3}$$

and

$$\frac{\partial \phi}{\partial t} + \nabla \cdot \mathbf{\Phi} = 0 \tag{4}$$

These equations are solved sequentially. The solution of eq. (3), which is advanced in time, is used. In eq. (4) the first term of left-hand side is a dummy value, since it's solved by keeping the time stopped.

2.1 Lagrangian Formulation

Equation (3) is the so-called Lagrangian step. So, the mass, momentum and energy conservation are solved in this step

$$\frac{\partial \rho}{\partial t} = 0 \tag{5}$$

$$\frac{\partial \rho \boldsymbol{v}}{\partial t} = \nabla \cdot \boldsymbol{\sigma} + \rho \boldsymbol{b} \tag{6}$$

$$\frac{\partial e}{\partial t} = \boldsymbol{\sigma} : \boldsymbol{D} \tag{7}$$

where ρ is the density of the material, $\boldsymbol{\sigma}$ is the Cauchy stress, $\boldsymbol{b}$ is the body force and $\boldsymbol{D}$ is the velocity strain. These equations are solved in standard Lagrange hydrocodes, in explicit as well in implicit time integration. For impact problems the explicit time integration is more attractive because of its suitability to parallel computing. No global stiffness matrix is necessary to solved, making it easier to code.

The discretized equation in explicit form using the central difference method is for the material acceleration $\boldsymbol{a}^n$, velocity $\boldsymbol{v}^{n+1/2}$ and coordinates $\boldsymbol{x}^{n+1}$

$$\boldsymbol{a}^n = \boldsymbol{M}^{-1}(\boldsymbol{F}^{ext} - \boldsymbol{F}^{int}) \tag{8}$$

$$\boldsymbol{v}^{n+1/2} = \boldsymbol{v}^{n-1/2} + \Delta t \boldsymbol{a}^n \tag{9}$$

$$\boldsymbol{x}^{n+1} = \boldsymbol{x}^n + \Delta t \boldsymbol{v}^{n+1/2} \tag{10}$$

where $\boldsymbol{M}$ is the nodal masses, $\boldsymbol{F}^{ext}$ nodal external forces and $\boldsymbol{F}^{int}$ are the nodal internal forces. Δt is the current time step.

2.2 Eulerian Advective Step

Equation (4) is often called the advective, convective or Eulerian step. This represents the material transport through the cells of the fixed Euler mesh. In the operator splitting method Eqs. (3) and (4) are solved sequentially. In order to extend existing traditional Lagrange FEM codes to an Eulerian formulation in a convenient way, practical-to-implement finite difference subroutines have been focused here. In this hydrocode, a monotonic, second order, cell-centered algorithm has been programmed for cell-centered solution variables, while a modification has been done for the momentum advection, which is vertex-centered. In this case, the vertex-centered momentum will be averaged to a cell-centered momentum, which is advected with the same algorithm for cell-centered variables. A final step is required, namely to extrapolate the cell-centered results to a vertex-centered ones [14) 15) 16)].

After the Lagrangian step, the deformed mesh is remeshed to the original place easily by setting nodal coordinates back. Here, it important to remember that the deformed mesh is not allow to have longer deformations than the element size. The Courant time step control method must take care of this.

Here the second order Van Leer's MUSCL (monotone upwind schemes for conservation laws) method is implemented. MUSCL method is a one-dimensional transport algorithm. In logically meshes the one-dimensional advection is carried out along the mesh lines.

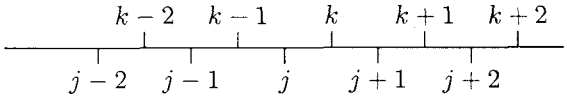

A solution variable f_k^- of a element k is advected to f_k^+ using following algorithm

$$f_k^+ = f_k^- + \frac{\Delta t}{\Delta x}(\Phi_j - \Phi_{j+1}) \tag{11}$$

where Φ values are fluxes. Indexes j and k represent vertex-centered and element-centered values, respectively. The flux is calculated as

$$\Phi_j = 0.5 v_j(\phi_j^- + \phi_j^+) + 0.5|v_j|(\phi_j^- - \phi_j^+) \tag{12}$$

where v_j is the velocity at nodal velocity at node j. ϕ values are calculated by

$$\begin{aligned} \phi_j^+ &= f_k + S_k \Delta x \\ \phi_j^- &= f_{k-1} + S_{k-1} \Delta x \end{aligned} \tag{13}$$

where the suffix + and - represent the variable values from the right and left side, respectively. The slope S is then

$$S_k = \tfrac{1}{2}(sgn(s_L) + sgn(s_R))\min(|s_L|, |s_C|, |s_R|)$$

$$\begin{aligned} s_L &= \tfrac{f_k - f_{k-1}}{\Delta x} \\ s_R &= \tfrac{f_{k+1} - f_k}{\Delta x} \\ s_C &= \tfrac{f_{k+1} - f_{k-1}}{2\Delta x} \end{aligned} \tag{14}$$

where a regular equidistant mesh is assumed. A extension for non-equidistant meshes is already done by many other authors.

3. Time Step Control

The time step used in this hydrocode refers that from LS-DYNA [4]

$$\Delta t = C_u \frac{L_s}{c_e + v_{max}} \tag{15}$$

where C_u is the Courant coefficient, L_s is a calculated length, c_e is the element wavespeed and v_{max} is the maximal velocity existing in system.

The Courant coefficients used here are 0.2 for quadrilaterals and 0.3 for hexahedras. However, for hypervelocity impact problems a reduction of the Courant coefficient in factors between 10 and 100 is necessary.

The calculated length L_s is then

$$L_s = \left\{ \begin{array}{ll} \frac{A_e}{d_{max}} & \text{for quadrilaterals} \\ \\ \frac{V_e}{A_{max}} & \text{for hexahedras} \end{array} \right\} \tag{16}$$

where A_e is the element area and d_{max} is the maximal distance between nodes. For hexahedras, V_e is the element volume and A_{max} is the biggest area of the hexahedras's sides.
The element wavespeed is

$$c_e = \sqrt{\frac{E}{(1-\nu^2)\rho}} \tag{17}$$

where E, ν and ρ are the young modulus, the Poisson ratio and density, respectively.

4. Radial Return Method for J_2 Flow Plasticity Theory

Metal plasticity is most simulated by using J_2 flow plasticity theory, which bases on a von Mises yield surface. The reason is that plastic flow in metals is not effected by pressure what has been experimentally confirmed.

For integrating rate constitutive equations, return mapping algorithms have been developed [1]. Since J_2 flow theory bases on von Misses yield surface, the general mapping algorithm reduces to the radial return algorithm.

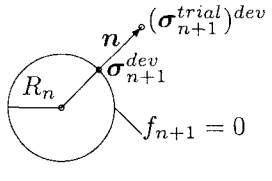

Fig. 1 Radial return method [1]

Figure 1 describes the radial return method. Elasticity keeps limited by the yield surface $f_{n+1} = 0$. If a stress value $(\boldsymbol{\sigma}_{n+1}^{trial})^{dev}$ overcross the yield surface outwards, it will be radially returned to the yield surface to $\boldsymbol{\sigma}_{n+1}^{dev}$.

The trial stress is purely elastic

$$\boldsymbol{\sigma}_{n+1}^{trial} = \boldsymbol{\sigma}_n + \boldsymbol{C}\Delta\boldsymbol{\epsilon} \tag{18}$$

The deviatoric part is then

$$(\boldsymbol{\sigma}_{n+1}^{trial})^{dev} = \boldsymbol{\sigma}_{n+1}^{trial} - \frac{1}{3} tr(\boldsymbol{\sigma}_{n+1}^{trial})\boldsymbol{I} \tag{19}$$

The von Misses stress is

$$A = (\boldsymbol{\sigma}_{n+1}^{trial})^{dev} \cdot (\boldsymbol{\sigma}_{n+1}^{trial})^{dev} \tag{20}$$

If $A \leq R_n^2$ then

$$\boldsymbol{\sigma}_{n+1} = \boldsymbol{\sigma}_{n+1}^{trial} \tag{21}$$

$$R_{n+1} = R_n \tag{22}$$

This is the case in which the stress does not abandon the yield surface. Plasticity occurs
by $A > R_n^2$

$$\boldsymbol{\sigma}_{n+1} = \boldsymbol{\sigma}_{n+1}^{trial} - 2\mu\tilde{\Lambda}\boldsymbol{n} \tag{23}$$

$$R_{n+1} = R_n + \frac{2}{3}H'\tilde{\Lambda} \tag{24}$$

where

$$\boldsymbol{n} = \frac{(\boldsymbol{\sigma}_{n+1}^{trial})^{dev}}{|(\boldsymbol{\sigma}_{n+1}^{trial})^{dev}|} \tag{25}$$

$$\tilde{\Lambda} = \frac{1}{2\mu\left(1 + \frac{H'}{3\mu}\right)} \left(|(\boldsymbol{\sigma}_{n+1}^{trial})^{dev}| - R_n\right) \tag{26}$$

The plastic strain tensor and the equivalente plastic strain are calculated by

$$\boldsymbol{\epsilon}_{n+1}^{p} = \boldsymbol{\epsilon}_n^{p} + \tilde{\Lambda}\boldsymbol{n} \tag{27}$$

$$\bar{\epsilon}_{n+1}^{p} = \bar{\epsilon}_n^{p} + \sqrt{\frac{2}{3}}\tilde{\Lambda} \tag{28}$$

5. Material and Fracture Model

Johnson and Cook [17] [18] concluded that material fracture does not only depend on the plastic strain but also on the plastic strain rate and temperature. High plastic strain rates are present in hypervelocity impact problems and therefore interesting to take in account. Based on their own experimental data, they developed the Johnson-Cook material and fracture model, where effects coming from plastic strain, plastic strain rate and temperature are separately arranged.

5.1 Johnson-Cook Material Model

The flow stress is given by

$$\sigma_y = [A + B\bar{\epsilon}^{p\,n}][1 + C ln\dot{\epsilon}^{p^*}][1 - T^{*^m}] \qquad (29)$$

where A, B, C, n, m are material constants extracted from experiments, $\bar{\epsilon}^p$ is the equivalent plastic strain, $\dot{\epsilon}^{p^*} = \dot{\epsilon}^p \;/\; \dot{\epsilon}_0^p$ is the dimensionless plastic strain rate for $\dot{\epsilon}_0^p = 1.0s^{-1}$ and

$$T^* = \frac{T - T_{room}}{T_{melt} - T_{room}} \qquad (30)$$

The first bracket block represents the effect due to plastic strain, as the second bracket block represents the plastic strain rate effect. The last bracket block is the material temperature effect.

5.2 Johnson-Cook Fracture Model

The strain at fracture is given by

$$\epsilon^f = [D_1 + D_2 e^{(D_3\sigma^*)}][1 + D_4 ln\dot{\epsilon}^{p^*}][1 + D_5 T^*] \quad (31)$$

where D_1 to D_5 are material constants and

$$\sigma^* = \frac{P}{\sigma_{eff}} \qquad (32)$$

is the ratio of pressure P divided by the effective stress σ_{eff}.

$$\sigma_{eff} = \sqrt{\frac{3}{2}\boldsymbol{\sigma} : \boldsymbol{\sigma}} \qquad (33)$$

where $\boldsymbol{\sigma}$ is the deviatoric Cauchy stress.

$\mathcal{D}$ is the accumulated damage paramater and $\Delta\bar{\epsilon}^p$ is the equivalent plastic strain increment Fracture occurs then when

$$\mathcal{D} = \sum \frac{\Delta\bar{\epsilon}^p}{\epsilon^f} \qquad (34)$$

reaches 1.0.

It is reported that fracture is very dependent on the state of hydrostatic pressure and less dependent on the strain rate and temperature [17]. To remark is here that this conclusion based on data from torsion and quasi-static tensile tests. However, results using this hydrocode showed the strong dependency of strain rate for hypervelocity problems.

6. Contact Algorithms

6.1 Penalty Method

The well-known penalty method for contact problems is robust and simple to implement. The concept of this method is to apply normal interface springs between penetrating nodes and contact surface. The spring forces are then treated as external forces in the system.

The contact force on a hitting node is given by

$$f^h = -\alpha g \boldsymbol{n} \qquad (35)$$

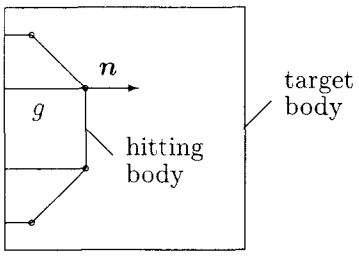

Fig. 2 Penalty method

there α is the penalty parameter, g is the penetration and $\boldsymbol{n}$ is the outwards normal vector to the contact surface. The contact force on the target body is then given by

$$\boldsymbol{f}_i^t = -N_i \boldsymbol{f}_i^h, \qquad i\text{=1,numnodes} \qquad (36)$$

where N are the element shape functions and numnodes is the number of nodes of the target element in which the hitting node is.

The calculation of contact forces are carried out for all hitting nodes inside of a target element.

Different from penetration constrained methods, the penalty method allows penetration. Therefore, the spring stiffness is to be scaled up as well the time step is scaled down to avoid unacceptable penetration by high-velocity problems.

6.2 Mixture Theory

Mixture theories concept the treatment of more than one material in an element. The simplest mixture theory have the assumption that the strain rate $\dot{\boldsymbol{\epsilon}}$ is same for all present materials in an element. So the stress rate $\dot{\boldsymbol{\sigma}}_m$ of material m is given by

$$\dot{\boldsymbol{\sigma}}_m = \boldsymbol{C}_m : \dot{\boldsymbol{\epsilon}} \qquad (37)$$

where $\boldsymbol{C}_m$ is the constitutive tensor of material m

The updated stress $\boldsymbol{\sigma}_m^{n+1}$ by time $n+1$ is then

$$\boldsymbol{\sigma}_m^{n+1} = \boldsymbol{\sigma}_m^n + \dot{\boldsymbol{\sigma}}_m \Delta t \qquad (38)$$

The element mean stress $\overline{\boldsymbol{\sigma}}^{n+1}$ is then

$$\overline{\boldsymbol{\sigma}}^{n+1} = \sum_{m=1}^{M} \boldsymbol{\sigma}_m^{n+1} f_m \qquad (39)$$

where M is the number of materials present in the element and f_m is the element filling rate of each material m.

The simplest mixture theory, also called the mean strain rate mixture theory, is favorized because of its simplicity and robustness even for high pressures and strain rates [13].

7. One-Point Element Integration

Explicit finite element programs are widely used for impact problems using very small time steps. In order to reduce the computational time low order elements with element reduced-integration are favorized.

However, the one-point quadrature element is rank deficient, i.e. it possesses spurious singular modes often called 'hourglass modes' which need to be stabilized. For this, hourglass stabilization procedures have been developed [1]. Here two hourglass control methods are reported.

The perturbation hourglass stabilization augments the rank of the element in two in order to restore the correct or proper rank of the element. A normalized hourglass parameter, which base on the eigenvalue of elements, is developed in order to augment the rank of the material constitutive tensor.

The physical hourglass stabilization has been developed on basis on assumed strain methods, which have the goal to avoid volumetric locking i.e it is suitable for nonlinear incompressible problems such as plasticity in metals. Different from the perturbation stabilization, the physical hourglass stabilization considers element material properties and geometry.

7.1 Element Rank

The element rank is defined by the number of nodes multiplicated by the number of degree of freedom each node. The proper element rank is defined by the element rank minus the number of rigid-body motions. For two dimensional calculations, a quadrilateral 4-node element has the proper rank of five as shown in Table 7.1

Table 1 Proper rank of a quadrilateral element

Element rank		=	8
number of element nodes	= 4		
degrees of freedom each node	= 2		
Rigid-body motions		=	3
translations	= 2		
rotations	= 1		
Element proper rank		=	5

The element integration is in strong dependency of the strain-displacement matrix B which is in two dimensional case of maximum rank three i.e. all tree rows of B are linear independent. Thus, the element has rank deficiency.

7.2 Element spurious singular modes

As seen from the brief review in Section 7.1, there are two so-called spurious singular modes or zero-energy modes which are shown in form of hourglass shapes and need to be resisted.

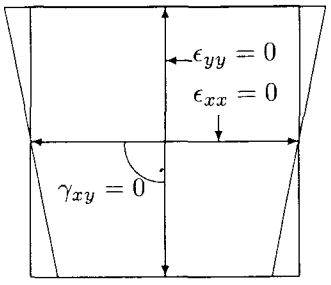

Fig. 3 Hourglass mode in x-direction

For the deformation case in which the nodes of an element move in the sequence; the top nodes move outwards and bottom one the same distance but inwards; we have the hourglass mode in x-direction as shown in Fig. 3. Regarding to the integration point there are neither change in the lengths nor rotation what means no strain change that is no stress. The rate-of-deformation at the quadrature point is given by

$$D(0) = B(0)\dot{d} \tag{40}$$

where

$$B(0) = \begin{bmatrix} bx & 0 \\ 0 & by \\ by & bx \end{bmatrix}$$

Let the nodal velocities $\dot{d}$ have following form

$$\dot{d}^{Hx} = \begin{Bmatrix} h \\ 0 \end{Bmatrix}, \quad h = \begin{Bmatrix} +1 \\ -1 \\ +1 \\ -1 \end{Bmatrix}$$

Then it is obviously that the rate-of-deformation in Equation 40 vanishes for $\dot{d}^{Hx}$. This produces the x-hourglass because of the motion in x-direction. Figure 4 shows a mesh in hourglass mode of deformation.

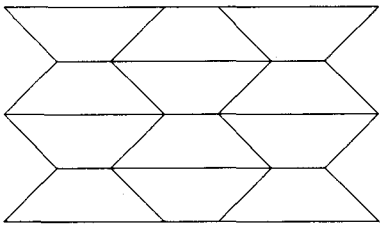

Fig. 4 Mesh in hourglass mode of deformation

7.3 Hourglass Control

(1) Perturbation hourglass stabilization

In perturbation hourglass control, the proper rank of element is restored by adding two rows to the B matrix. To ensure the linearly independence, the new rows are orthogonal to the other three. The element matrices are then

$$\tilde{\boldsymbol{B}} = \begin{bmatrix} \boldsymbol{b_x} & \boldsymbol{0} \\ \boldsymbol{0} & \boldsymbol{b_y} \\ \boldsymbol{b_y} & \boldsymbol{b_x} \\ \boldsymbol{\gamma} & \boldsymbol{0} \\ \boldsymbol{0} & \boldsymbol{\gamma} \end{bmatrix}$$

$$[\tilde{\boldsymbol{C}}] = \begin{bmatrix} C_{11} & C_{12} & C_{13} & 0 & 0 \\ C_{21} & C_{22} & C_{23} & 0 & 0 \\ C_{31} & C_{32} & C_{33} & 0 & 0 \\ 0 & 0 & 0 & C^Q & 0 \\ 0 & 0 & 0 & 0 & C^Q \end{bmatrix}$$

where

$$\boldsymbol{\gamma} = \frac{1}{4}(\boldsymbol{h} - (\boldsymbol{h}^T\boldsymbol{x})\boldsymbol{b}_x - (\boldsymbol{h}^T\boldsymbol{y})\boldsymbol{b}_y)$$

and

$$\boldsymbol{h}^T = [+1 \; -1 \; +1 \; -1]$$

$$\tilde{\boldsymbol{\sigma}} = \begin{Bmatrix} \sigma_x \\ \sigma_y \\ \sigma_{xy} \\ Q_x \\ Q_y \end{Bmatrix} \quad \tilde{\boldsymbol{D}} = \begin{Bmatrix} D_x \\ D_y \\ 2D_{xy} \\ \dot{q}_x \\ \dot{q}_y \end{Bmatrix}$$

where

γ is the orthogonal vector
C^Q is a parameter (not true material constant)
Q_x and Q_y are hourglass stresses
$\dot{q}_x$ and $\dot{q}_y$ are hourglass velocity strains

Stabilization procedure

The internal nodal forces for the stabilized element are

$$\begin{aligned} \boldsymbol{f}^{int} &= A\tilde{\boldsymbol{B}}^T\tilde{\boldsymbol{\sigma}} \qquad \overbrace{\qquad\qquad}^{\boldsymbol{f}^{stab}} \\ &= AB^T\boldsymbol{\sigma} \quad + \quad \overbrace{A\begin{Bmatrix} Q_x\gamma \\ Q_y\gamma \end{Bmatrix}} \end{aligned} \tag{41}$$

The hourglass velocity strain are calculated by

$$\dot{q}_x = \boldsymbol{\gamma}^T\boldsymbol{v}_x, \quad \dot{q}_y = \boldsymbol{\gamma}^T\boldsymbol{v}_y \tag{42}$$

The hourglass stress rates are calculated by

$$\dot{Q}_x = C^Q\dot{q}_x, \quad \dot{Q}_y = C^Q\dot{q}_y, \tag{43}$$

The hourglass parameter C_Q is calculated by

$$C^Q = \frac{1}{2}\alpha_s c^2 \rho A \boldsymbol{b}_i^T\boldsymbol{b}_i \tag{44}$$

Notice that C^Q is a not true material constant, it is normalized to provide good results for any geometry and any material. Belytschko and Bindeman (1991) selected C^Q so the maximum eigenvalue of the stabilization stiffness is scaled to the maximum eigenvalue of the under-integrated stiffness. The recommended values for α_s are about 0.1 [1].

Anyway this value does not avoid hourglass for complete. In cases where the date is rich of hourglass mode, it is difficult to suppress the hourglass mode even with large values of the stabilization parameter. Point loads for example are often causing hourglassing. In cases where hourglass mode appears inexplicably and there is no solution for a stabilization, it is better to switch to a fully integrated element in those sub-domain where it appears.

Flowchart of perturbation hourglass control

1. Compute hourglass velocity strains by Eq. (42)
2. Compute parameter C^Q by Eq. (44)
3. Compute hourglass stresses $Q_i = \dot{Q}_i\Delta t$ by Eq. (43)
4. Update internal nodal forces by Eq. (41)

(2) Physical hourglass stabilization

Hourglass stabilization procedures have been developed on the basis of assumed strain methods [8) 9)]. In these procedures, the stabilization parameters are based on the material properties and geometry of the element. Assumed strain methods are developed for avoiding volumetric locking. Thus, physical hourglass stabilization is suitable for nonlinear incompressible problems such as plasticity in metals.

Stabilization procedure

For physical hourglass stabilization procedure two assumptions must be made:

- the spin is constant within the element
- the material response is uniform within the element

A velocity field has been developed in order to avoid locking [10)]

$$v_i = (\bar{\mathbf{1}}^T\boldsymbol{v}_i) + (\boldsymbol{b}_x^T\boldsymbol{v}_i)x + (\boldsymbol{b}_y^T\boldsymbol{v}_i)y + (\boldsymbol{\gamma}^T\boldsymbol{v}_i)h \tag{45}$$

where

$$\bar{\mathbf{1}}^T = [1 \;\; 1 \;\; 1 \;\; 1]$$
$$h = \xi\eta$$

The velocity strain is then

$$\boldsymbol{D} = \begin{Bmatrix} \boldsymbol{b}_x + h_{,x}\boldsymbol{\gamma} & 0 \\ 0 & \boldsymbol{b}_y + h_{,y}\boldsymbol{\gamma} \\ \boldsymbol{b}_y + h_{,y}\boldsymbol{\gamma} & \boldsymbol{b}_x + h_{,x}\boldsymbol{\gamma} \end{Bmatrix} \begin{Bmatrix} \boldsymbol{v}_x \\ \boldsymbol{v}_y \end{Bmatrix} \tag{46}$$

The hourglass stress rate is

$$\dot{\boldsymbol{\sigma}}^H = \left\{ \begin{array}{c} C_1\dot{q}_x h_{,x} + C_2\dot{q}_y h_{,y} \\ C_2\dot{q}_x h_{,x} + C_1\dot{q}_y h_{,y} \\ C_3(\dot{q}_y h_{,x} + \dot{q}_x h_{,y}) \end{array} \right\} \tag{47}$$

The hourglass stabilization forces are then

$$\boldsymbol{f}^{stab} = \left\{ \begin{array}{l} C_1\dot{q}_x H_{xx} + C_2\dot{q}_y H_{xy} \\ +C_3(\dot{q}_y H_{yx} + \dot{q}_x H_{yy}) \\ \\ C_2\dot{q}_x H_{yx} + C_1\dot{q}_y H_{yy} \\ +C_3(\dot{q}_y H_{xx} + \dot{q}_x H_{xy}) \end{array} \right\} \gamma\Delta t \tag{48}$$

where

$$H_{x_i x_j} = \int_\Omega h_{x_i} h_{x_j} d\Omega \tag{49}$$

Following integrals are solved using Gauss integration

$$\begin{array}{rcl} \int_{-1}^{+1}\int_{-1}^{+1} \xi^2 J d\xi d\eta & = & \int_{-1}^{+1} [\xi^2\eta]_{-1}^{+1} J d\xi \\ & = & \int_{-1}^{+1} 2\xi^2 J d\xi \\ & = & [2\frac{\xi^3}{3}]_{-1}^{+1} J = \frac{4J}{3} = \frac{A}{3} \end{array} \tag{50}$$

the same for

$$\int_{-1}^{+1}\int_{-1}^{+1} \eta^2 J d\xi d\eta = \frac{A}{3} \tag{51}$$

and

$$\int_{-1}^{+1}\int_{-1}^{+1} \xi\eta J d\xi d\eta = \int_{-1}^{+1} [\xi\frac{[\eta]^2}{2}]_{-1}^{+1} J d\xi = 0 \tag{52}$$

Equation (49) can be formed in a programming friendly way as

$$\begin{array}{rcl} H_{x_i x_j} & = & \frac{A}{3}\left(x_{iI}\frac{\partial N_I}{\partial\xi}\right)^{-1}\left(x_{jI}\frac{\partial N_I}{\partial\xi}\right)^{-1} \\ & + & \frac{A}{3}\left(x_{iI}\frac{\partial N_I}{\partial\eta}\right)^{-1}\left(x_{jI}\frac{\partial N_I}{\partial\eta}\right)^{-1} \end{array} \tag{53}$$

Both, perturbation and physical hourglass control methods have been implemented. However, physically calculated stabilization forces gives more accurate results. Computational results showed the robustness of the physical hourglass control by reducing the computational time enormously.

Flowchart of physical hourglass control

1. Compute hourglass velocity strains by Eq. (42)
2. Compute $H_{x_i x_j}$ values by Eq. (53)
3. Compute hourglass forces by Eq. (48) and update internal forces

8. Computational Results

Several contact-impact tests have been carried out. The tests are: a Taylor impact bar, a tube impact, a coining tool-workpiece model and a high-speed contact-impact test. Both Lagrangian and Eulerian meshes have been used. Both contact algorithms, penalty method and mixture theory are used in these tests. The Courant number has been reduced for high-speed problems.

8.1 Taylor Projectile-Target Test

The penalty method shows an ignorable minimal penetration by the famous Taylor impact bar. Both, projectile and target is modeled and calculated in Lagrange mode. The target is in this case a rigid foundation. The impact speed is 300m/s. The 1.5x6.0cm modeled is model with a 10x20 mesh. Material properties of the impact bar are listed in table 2.

Table 2 Impact bar: material properties

Young modulus (GPa)	218.75
Density (kg/m^3)	7800
Poisson's ratio	0.2868
Yield stress (MPa)	200
Hardening modulus	0.01

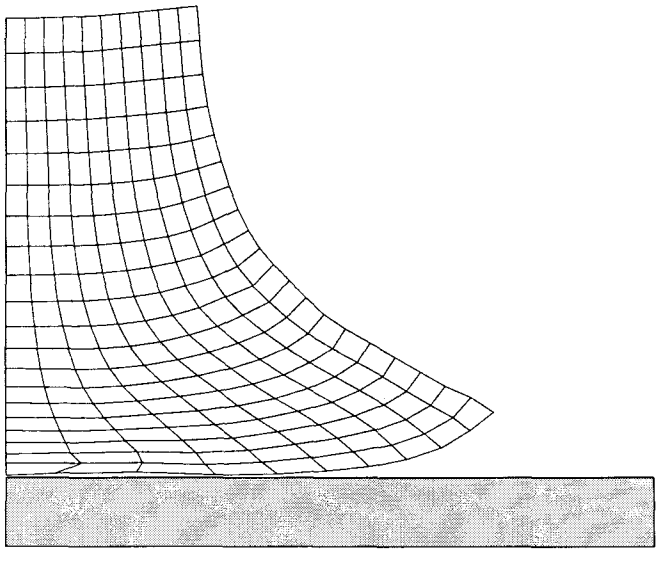

Fig. 5 Taylor projectile-target plot by 75 μs

The Taylor impact bar is famous because of its sensibility against hourglassing, volumetric locking and contact forces. As shown in Fig. 5 none of these problems occurs which confirms the well-working of the hourglass control and penalty method.

8.2 Tube Impact Test

A tube of 100cm radius and 10cm thickness impacts down with 50m/s onto a rigid foundation which is modeled by one element. The tube model uses plane strain elements. Deformation plots by 0, 5, 10 and 15 milliseconds are shown in fig. 6. Both, no hour-glassing occurs and a clean contact demonstration is reached. The penalty method shows here also no penetration. is visible. Material properties of the impact tube are listed in table 3.

Table 3 Tube Impact: material properties

Young modulus (GPa)	200
Density (kg/m^3)	7800
Poisson's ratio	0.3
Yield stress (MPa)	100
Hardening modulus	0

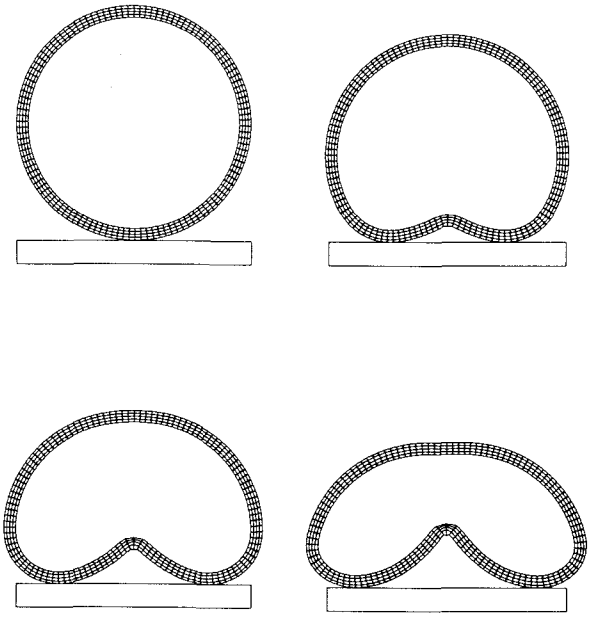

Fig. 6 Tube impact

8.3 Coining Test

The advantage of an Eulerian mesh by large mesh deformation is shown in Fig. 7 and Fig. 8. The tool is modeled and calculated in Lagrangian mode. The workpiece is modeled in Lagrangian mode, Fig. 7 and in Eulerian as well, Fig. 8. In both cases, penalty forces control the contact. For the Lagrangian model, the workpiece is model with a 50x16 mesh. The Eulerian model dimension is 5.0x3.0cm and is meshed by using a 50x30 mesh.

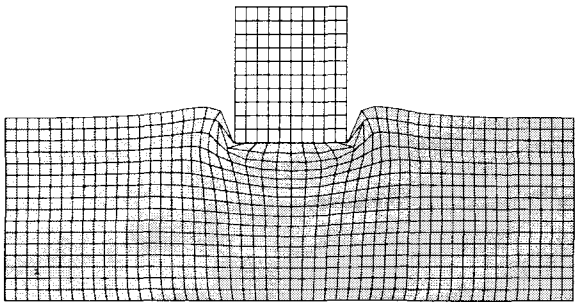

Fig. 7 Coining with Lagrangian mesh

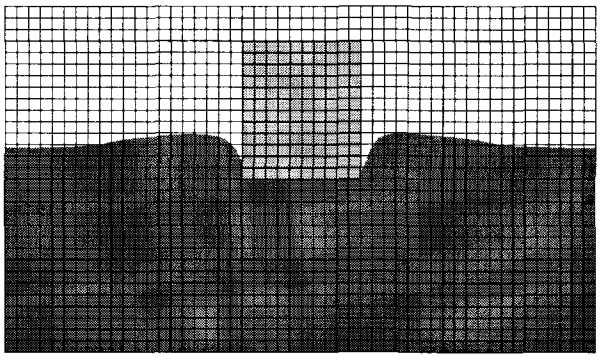

Fig. 8 Coining with Eulerian mesh

8.4 High-Speed Impact Test

High-speed contact-impact simulations in Eulerian formulation have been carried out and reported here. Both, the projectile and the target are aluminum. Figure 9 shows results of a square-projectile of $1cm^2$ with an impact velocity of 1cm/μs. Impact plots by using VISTA, a particle-in-cell(PIC) code, are presented in [5]. In Fig. 10, the projectile of aluminum hits the 2-layer target with speed of 1.5 cm/μs. The first and second layer are of plexiglass and aluminum, respectively. Figure 11 shows results of a circular-projectile of $1cm$ radius with an impact velocity of 0.618cm/μs.

The theory of high-speed impact covers a broad number of topics like high pressure and temperature effects, high strain rates, large material deformation or distortion and stress shock waves. An estimation of shock waves soon after impact, Fig. 12 (top), and after reflection of shock from target face, 12 (bottom) is presented [5]. Results showed in Fig. 13 match well with expected shock waves propagation as well with the rearward material ejection. The rearward ejection of projectile and target material is well demonstrated with the velocity vector in rearward direction. Further,the projectile velocity flows into the target.

Fig. 9 Projectile-target plots by 0.0, 1.0 and 2.0μs

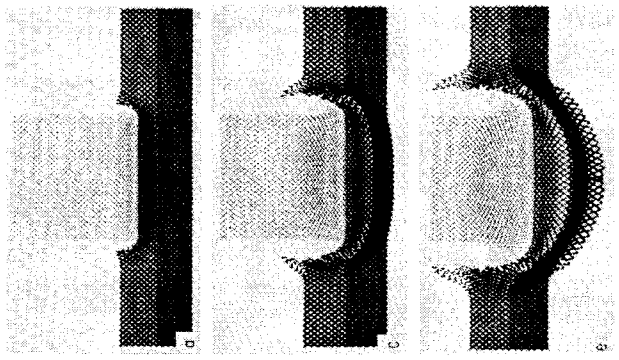

Fig. 10 Projectile-target plots by 0.05, 0.10, 0.15μs [5)]

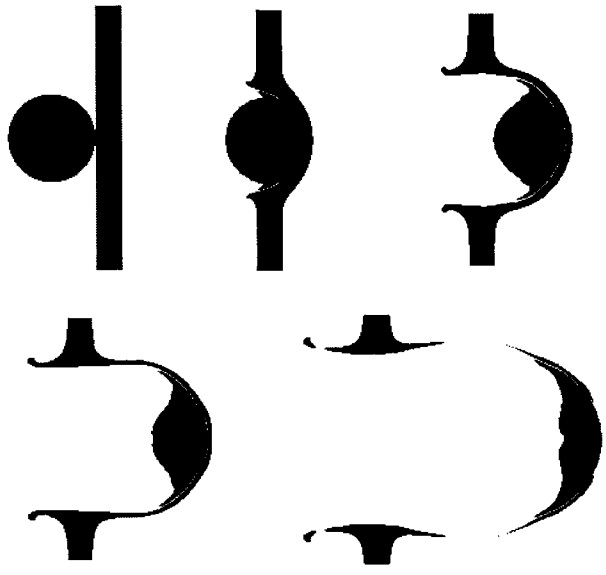

Fig. 11 Cirlular projectile-target plots by 0.0, 1.0, 2.0, 3.0 and 5.0μs

Johnson-Cook fracture model is well simulated, as shown in Fig. 11. New material shapes are shown in the plot by 5.0μs. Refining the mesh and reducing the limit of the filling rate (0.5 used here) will display more small separated shapes.

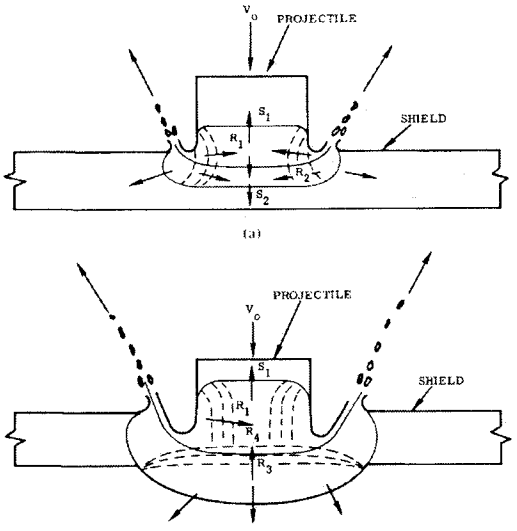

Fig. 12 Estimate wave pattern [5)]

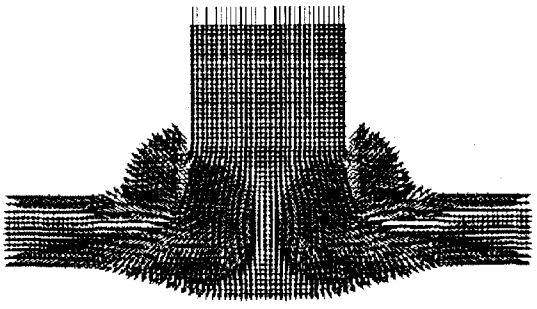

Fig. 13 Velocity field

An equivalent plastic strain plot by 1.0μs belonging to the circular projectile-target impact test is presented in Fig. 14.

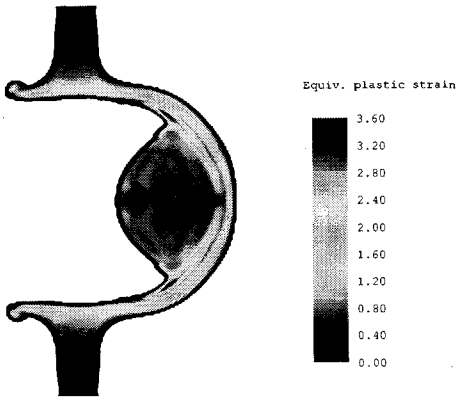

Fig. 14 Equivalent plastic strain by 1.0μs

9. Conclusion

Computational results have shown the success of present contact-impact procedure. The quality of these numerical results match well with references. A remarkable computational time performance has been reached by implementing 1-point quadrature elements with physical hourglass control method, keeping good accuracy and avoiding hourglassing. J_2 flow plasticity theory with radial return method has shown once more its suitability to metal plasticity. Further, results showed the robustness of the penalty method for contact problems in Lagrangian meshes as well the implemented mixture theory for Eulerian meshes.

Here is shown the suitability of Eulerian hydrocodes for high-speed contact-impact problems, where high pressures and strain rates are well simulated by using Johnson-Cook material model. Eulerian hydrocodes allow automatically new free-surface creation and solve the problem of mesh distortion. However, other methods, specially smooth particle hydrodynamics are shown in the literature as very promising.

REFERENCES

1) Belytschko T., Liu W. K., Moran B.: *Nonlinear Finite Elements for Continua and Structures*, John Wiley 2000
2) Holzapfel G.A.: *Nonlinear Solid Mechanics*, John Wiley 2001
3) Bonet J., Wood R.D.: *Nonlinear Continuum Mechanics for Finite Element Analysis*, Cambridge University Press 1997
4) Hallquist, J. O.: *LS-DYNA Theoretical Manual*, Livermore Software Technology Corporation, May 1998
5) Kinslow R: *High-Velocity Impact Phenomena*, Academic Press, Inc. 1970
6) Libersky L.D, Petschek A.G.: High Strain Lagrangian Hydrodynamics. *Journal of Computational Physics*, Vol. 109, pp.67-75, 1993.
7) Petschek A.G., Libersky L.D.: Cylindrical Smoothed Particle Hydrodynamics *Journal of Computational Physics*, Vol. 109, pp.76-83, 1993.
8) Belytschko T., Leviathan I.: Physical stabilization of the 4-node shell element with one point quadrature. *Computer Methods in Applied Mechanics and Engineering*, Vol. 113, pp.321-350, 1994.
9) Belytschko T., Bindeman L.P.: Assumed strain stabilization of the 4-node quadrilateral with 1-point quadrature for nonlinear problems. *Computer Methods in Applied Mechanics and Engineering*, Vol. 88, pp.311-340, 1991.
10) Belytschko T., Bachrach W.E.: Efficient implementation of quadrilaterals with high coarse-mesh accuracy. *Computer Methods in Applied Mechanics and Engineering*, Vol. 54, pp.279-301, 1986.
11) Belytschko T., Bindeman L.P.: Assumed strain stabilization of the eight node hexahedral element. *Computer Methods in Applied Mechanics and Engineering*, Vol. 105, pp.225-260, 1993.
12) Albes de Sousa R.J., Natal J., Fontes V.: A new volumetric and shear locking-free 3D enhanced strain element. *Engineering Computations*, Vol. 20, pp.896-925, 2003.
13) Benson D. J.: An implicit multi-material Eulerian formulation. *International Journal for Numerical Methods in Engineering*, Vol. 48, pp.475-499, 2000.
14) Benson D.J.: Momentum advection on a staggered mesh. *Journal of Computational Physics*, Vol. 100, pp.143-162, 1992.
15) Benson D.J.: Computational methods in Lagrangian and Eulerian Hydrocodes. *Computer Methods in Applied Mechanics and Engineering*, Vol. 99, pp.235-394, 1992.
16) Van Leer B.: Towards the ultimative conservative difference scheme. IV. A new approach to numerical convection. *Journal of Computational Physics*, Vol. 23, pp.276-299, 1977.
17) Johnson G.R., Cook W.H.: Fracture characteristics of three metals subjected to various strains, strain rates, temperatures and pressures. *Engineering Fracture Mechanics*, Vol. 21, pp.31-48, 1985.
18) Johnson G.R., Cook W.H.: A constitutive model and data for metals subjected to large strains, high strain rates and high temperatures. *Proceeding of 7th International Symposium on Ballistics*, pp.541-547, 1983.
19) Zhi-Hua Z.: *Finite element procedures for contact-impact problems*, Oxford University Press 1993
20) Benson D.J., Okazawa S.: Contact in multi-material Eulerian finite element formulation. *Computer Methods in Applied Mechanics and Engineering*, Vol. 193, pp.4277-4298, 2004.
21) Doig R., Okazawa S.: Contact with a coupled Eulerian-Lagrangian hydrocode. *10th Conference of the Japan Society for Computational Engineering and Science, Tokyo May 2005*, Vol. 10, pp.183-186, 2005.

(Received April 15, 2005)